$Co(NO_3)_2$ as an inverted umbrella-type chiral non-coplanar ferrimagnet

I.L. Danilovich,[1] E.B. Deeva,[1] K.Y. Bukhteev,[1] A.A. Vorobyova,[1] I.V. Morozov,[1] O.S. Volkova,[1,2] E.A. Zvereva,[1,3] O.V. Maximova,[1,4] I.V. Solovyev,[2,5,6] S.A. Nikolaev,[6,7] D. Phuyal,[8] M. Abdel-Hafiez,[8,9] Y.C. Wang,[10] J.-Y. Lin,[10,11] J.M. Chen,[12] D.I. Gorbunov,[13] K. Puzniak,[14] B. Lake,[14,15] A.N. Vasiliev[1,2,3]

[1]Lomonosov Moscow State University, Moscow 119991, Russia
[2]Ural Federal University, Yekaterinburg 620002, Russia
[3]National Research South Ural State University, Chelyabinsk 454080, Russia
[4]National University of Science and Technology "MISiS", Moscow 119049, Russia
[5]Institute of Metal Physics, Yekaterinburg 620108, Russia
[6]MANA, National Institute for Materials Science, Tsukuba, Ibaraki 305-0044, Japan
[7]Tokyo Institute of Technology, Yokohama 226-8503, Japan
[8]Uppsala University, Uppsala SE-75120, Sweden
[9]Harvard University, Cambridge, Massachusetts 02138, USA
[10]National Chiao Tung University, Hsinchu 30010, Taiwan
[11]Center for Emergent Functional Matter Science, National Chiao Tung University, Hsinchu 30010, Taiwan
[12]National Synchrotron Radiation Center, Hsinchu 30076, Taiwan
[13]Hochfeld-Magnetlabor Dresden (HLD-EMFL), Helmholtz-Zentrum Dresden-Rossendorf, 01328 Dresden, Germany
[14]Helmholtz-Zentrum Berlin für Materialien und Energie GmbH, Berlin D-14109, Germany
[15]Berlin Technical University, Berlin D-10623, Germany

The low-dimensional magnetic systems tend to reveal exotic spin liquid ground states or form peculiar types of long-range order. Among systems of vivid interest are those characterized by the triangular motif in two dimensions. The realization of either ordered or disordered ground state in triangular, honeycomb or kagome lattices is dictated by the competition of exchange interactions, also being sensitive to anisotropy and the spin value of magnetic ions. While the low-spin Heisenberg systems may arrive to a spin liquid long-range entangled quantum state with emergent gauge structures, the high-spin Ising systems may establish the rigid non-collinear structures. Here, we present the case of chiral non-coplanar inverted umbrella-type ferrimagnet formed in cobalt nitrate $Co(NO_3)_2$ below T_C = 3 K with the comparable spin and orbital contributions to the total magnetic moment.

Introduction

Magnetic systems with reduced dimensionality are the intense focus of modern physics promising new insights into various quantum cooperative phenomena. Within this multitude, the layered compounds with triangular motif attract the utmost attention [1-3]. Similar to quasi-one-dimensional magnets, the triangular [4], honeycomb [5], and kagome [6] spin lattices may host an elusive spin liquid state whose properties are mostly defined by fine details of the underlying crystal structure. Along with disordered liquids, the layered and chain magnets may also form peculiar magnetic structures stabilized by interlayer or interchain interactions [7]. Among these structures is nickel nitrate $Ni(NO_3)_2$, a non-collinear umbrella-type ferrimagnet stabilized due to the competition of multiple antiferromagnetic exchange interactions [8].

In variance with conventional collinear Lieb-Mattis ferrimagnetism [9] which follows from incomplete cancellation of two inequivalent antiferromagnetically coupled sublattices, the non-collinear ferrimagnetism in $Ni(NO_3)_2$ stems from the frustration of antiferromagnetic interactions on the kagome lattice. The unconventional ferrimagnetism is realized, in particular, in the layers of six-sublattices buckled kagome antiferromagnets $Cu_3Bi(SeO_3)_2O_2X$ (X = Br, Cl)

due to geometrical frustration and Dzyaloshinsky-Moriya anisotropy [10]. Interestingly, the magnetic structure similar to umbrella-type ferrimagnet is also formed in the α-phase of elementary manganese by strongly magnetic Mn1 and Mn2, weakly magnetic Mn3 and nearly non-magnetic Mn4 atoms due to frustration of antiferromagnetic coupling of Mn4 [11].

Cobalt nitrate $Co(NO_3)_2$ belongs to a large family of anhydrous metal nitrates [12]. While these salts of alkali and alkaline earth metals are chemically stable, 3*d* transition metal nitrates are quite hygroscopic [13]. Until recently, this instability has prevented any thorough studies of numerous transition metal nitrates. Here, we present the results of experimental and theoretical study of $Co(NO_3)_2$ (Fig. 1), isostructural to its nickel counterpart, as obtained in measurements of both thermodynamic and resonant properties, X-ray absorption near edge structure (XANES) spectroscopy, and electronic structure calculations.

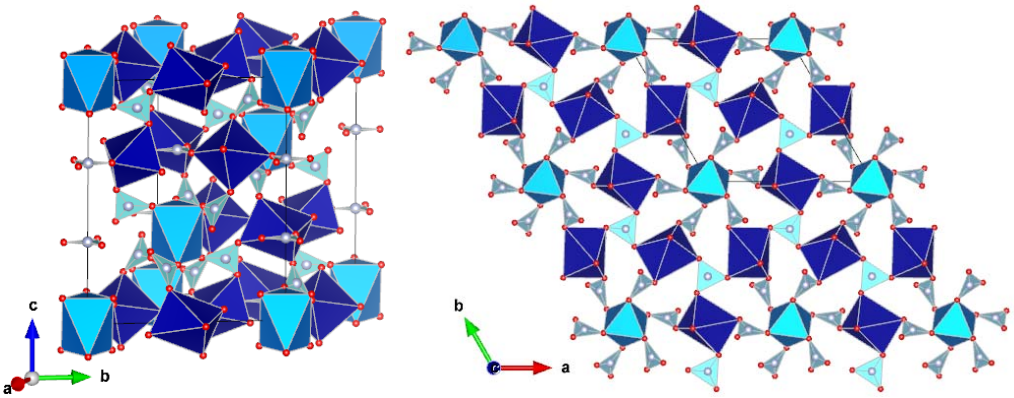

Fig. 1. Crystal structure of $Co(NO_3)_2$ in the polyhedral representation, visualized with VESTA software: ● Co1 ● Co2 ● N ● O [14].

Experimental

The title compound $Co(NO_3)_2$ in the form of a violet fine-crystalline powder was obtained by gradually heating a 0.5 g sample of $NO[Co(NO_3)_3]$ from 25° to 140° C for two hours under dynamic vacuum (0.01 mm Hg). Precursor $NO[Co(NO_3)_3]$ was obtained according to Ref. [15]. Purity of the obtained $Co(NO_3)_2$ sample was confirmed by Cu K_α X-ray diffraction. Due to the strong hygroscopicity of $NO[Co(NO_3)_3]$ and $Co(NO_3)_2$, the procedures associated with the preliminary preparations as well as recovery of the reaction product and its storage were performed in a glove box in an atmosphere of dry argon, with a moisture content not higher than 0.1 ppm. $Co(NO_3)_2$ crystallizes in the rhombohedral $R\bar{3}$ space group with a = 10.500(2) A, c = 12.837(3) A and Z = 12 [16]. The crystal structure of $Co(NO_3)_2$ is shown in Fig. 1. There are two non-equivalent positions of the Co^{2+} ions in the structure of cobalt (II) nitrate, the occupation of these positions is in the ratio of Co1:Co2 = 3:1. The CoO_6 octahedra linked through the regular and isosceles NO_3 triangles constitute the framework structure. The regular $N1O_3$ triangles link the Co1 ions into perfect kagome layers in the *ab* plane. This network hosts the Co2 ions lying in the hexagonal voids. The Co2 ions are linked with Co1 ions through the isosceles $N2O_3$ triangles. The successive kagome layers shifted by quarter periods along the *a* and *b* axes are coupled by $N2O_3$ groups along the *c* axis. The cobalt ions in $Co(NO_3)_2$ form two different CoO_6 octahedra. The pairwise Co1–O bond lengths in the distorted $Co1O_6$ octahedra are 0.2076(1), 0.2092(1) and 0.2136(1) nm, the Co2–O bond lengths in the regular $Co2O_6$ octahedra are 0.2123(1) nm [16].

$Co(NO_3)_2$ was characterized in measurements of thermodynamic and resonant properties. The field and temperature dependences of the magnetization M were taken by "Quantum Design" Magnetic Properties Measurements System MPMS-7T in a magnetic field up to B = 7 T in the temperature range T = 2 – 300 K. High-field magnetization was measured between 1.5 and 30 K in pulsed magnetic fields up to 58 T by the induction method using a coaxial pick-up coil system [17]. The sample has been cooled in zero magnetic field. Then, when the temperature was stable, a pulsed magnetic field was applied. Absolute values of the magnetization were

calibrated using data obtained in static fields. The temperature dependence of specific heat C_p was measured by "Quantum Design" Physical Properties Measurements System PPMS-9T employing the relaxation mode. Electron spin resonance spectra for powder samples of $Co(NO_3)_2$ were recorded by using an X-band ESR spectrometer CMS 8400 Adani (f = 9.5 GHz, $B \leq 0.7$ T) equipped with a low temperature mount. The effective g-factor has been calculated with respect to a BDPA reference sample with g_{ref} = 2.0035. To define the spin and oxidation states of the cobalt ions at room temperature, the X-ray absorption near-edge spectroscopy, XANES, at the cobalt $L_{2,3}$ and K edges has been employed. Co $L_{2,3}$ experiments were performed at the H-SGM beamline at the National Synchrotron Radiation Research Center in Taiwan. The data were taken in the total electron yield mode in an ultrahigh vacuum chamber. The photon energy resolution was 0.2 eV.

X-ray absorption spectroscopy

Since the compound under study was quite sensitive even to a short exposure to atmosphere, the XANES studies were performed after measurements of various physical properties. The Co XANES L-edge spectra measured at 300K are shown in the left panel of Fig. 2 for both CoO and $Co(NO_3)_2$. It is noted by the peak energy that the valence state of the Co ions in $Co(NO_3)_2$ remains 2+ as that of CoO. In order to obtain more details from the spectra, we have calculated the Co^{2+} L-edge spectra using the configuration interaction cluster model. This theoretical approach is based on atomic multiplet theory and local effects of the solid. The upper panel of Fig. 2 shows the measured spectrum of Co(NO3)2 compared with the simulations results with the contributions from the Co1 and Co2 ions. From the comparative results, it is clear that the shoulder A comes from Co1; both peaks B and C are from the combined contribution of Co1 and Co2. Feature D most likely originates from the contribution of Co1. Intriguingly, the simulated spectrum mimics very well the experimental one of $Co(NO_3)_2$ with an increased full width at half maximum (FWHM) for the simulated components. The information of the electron occupation and spin state is also available from the simulations. The simulated spectra of Co1 and Co2 in the left panel of Fig. 2 are obtained with the electron occupation in the value of $S(S+1)$ to be 3.7453 and 3.7449 for Co1 and Co2. Both values are very close to the high spin value of 3.75 for Co^{2+} $[Ar]3d^7$. Overall, the XAS combined with simulations convincingly show a high spin system in $Co(NO_3)_2$.

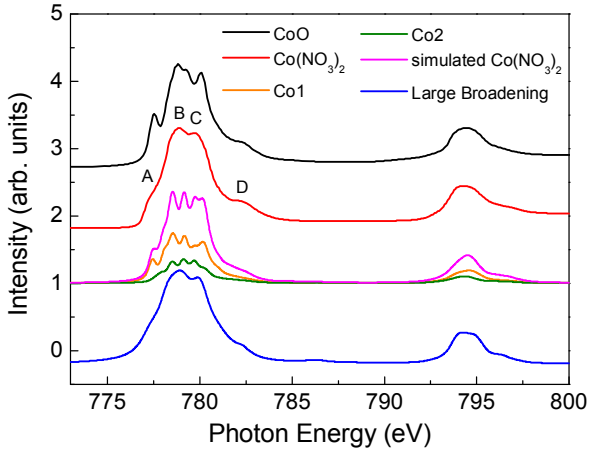

Fig. 2. L-edge spectra of CoO and $Co(NO_3)_2$, and the simulated spectrum of $Co(NO_3)_2$. The spectra from top to bottom are CoO, $Co(NO_3)_2$, simulated $Co(NO_3)_2$ (pink) with Co1 (orange) and Co2 (green) contributions, and the enlarged broadening simulated spectra.

X-band electron spin resonance.

Over the entire investigated temperature range, the typical ESR absorption signal of powder samples of $Co(NO_3)_2$ represents a distinct asymmetric mode, whose intensity increases

upon cooling the sample. For a S = 3/2 spin system (high spin Co^{2+}, d^7) in the octahedral environment, the zero field perturbation splits the energy levels into two doublets, $|\pm 1/2\rangle$ and $|\pm 3/2\rangle$. Thus, the absorption line could be assigned to the transitions in the ground state Kramers doublet with an anisotropic g-factor, which is assumed to originate from an excited doublet with the effective spin 3/2 [18]. The available data does not allow to resolve possible differences between the Co1 and Co2 signals.

In order to obtain quantitative estimations for the effective g-factors, we have fitted the experimental spectrum. Reasonable description of the ESR lineshape can be achieved by summing two Lorentzians. Representative example of the spectrum decomposition into resolved components is shown in the inset to Fig. 3. Temperature dependences of the parameters obtained from the lineshape analysis are shown in of Fig. 3. The principal values of the g-tensor were found to be $g_\perp$ = 4.16(2) and $g_{||}$ =4.01(3), giving $2g_\perp + g_{||} \approx 12.33$ in good agreement with the value of about 13 calculated in Ref. [19] for high-spin Co^{2+} (S=3/2) in the octahedral oxygen coordination. Both effective g-factor and the ESR linewidth vary weakly with temperature down to helium temperature. The integral ESR intensity, which is proportional to the number of magnetic spins, was estimated by double integration of the experimental dP/dB(B) line. It follows the Curie-Weiss-type behavior quantified in static magnetic susceptibility measurements.

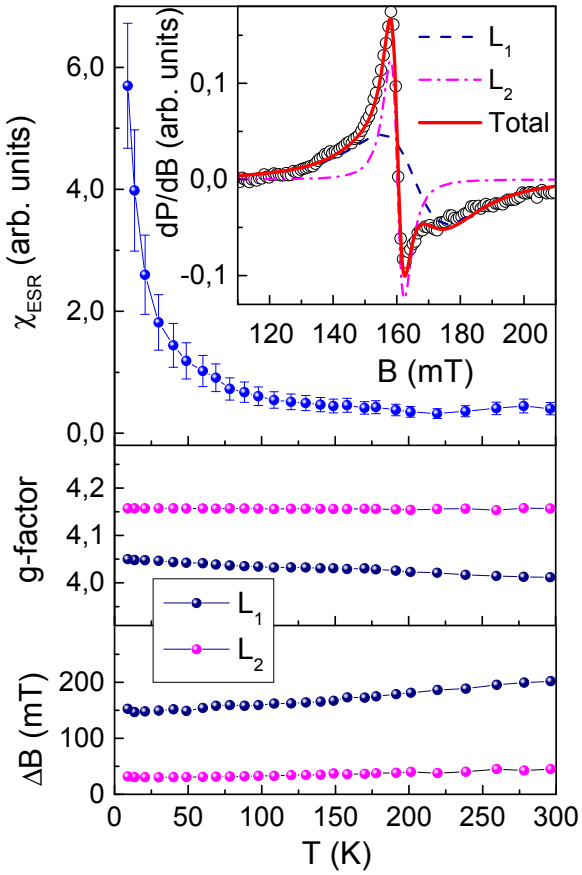

Fig. 3. Temperature dependences of the integral ESR intensity, effective g-factors and ESR linewidth for $Co(NO_3)_2$. The inset represents an example of the spectrum decomposition.

Thermodynamics

Over a wide temperature range, specific heat C_p in $Co(NO_3)_2$ was shown to follow the Debye function $D(T)$ which allows estimating the Debye temperature as $\Theta_D \sim 340$ K. The long range magnetic order in the title compound has been demonstrated in specific heat measurements through the formation of a sharp λ-type anomaly at T_C = 3 K, as shown in the upper panel of Fig. 4. The difference between the experimental data and Debye function was used to estimate the

magnetic entropy S_{mag} released at this transition. The S_{mag} vs. T dependence is shown in the inset to the upper panel of Fig. 4. Evidently, the quantity obtained at T_C is small as compared to the thermodynamic expectation $R\ln(2S+1)$ = 11.5 J/mol K. This indicates that a significant portion of the magnetic entropy is released above the phase transition, which agrees with the reduced dimensionality and frustration in the magnetic subsystem in $Co(NO_3)_2$.

Temperature dependence of *dc* magnetic susceptibility $\chi = M/B$ of $Co(NO_3)_2$ taken at B = 0.1 T is shown in the middle panel of Fig. 4. At high temperatures, it follows the Curie-Weiss law corrected by the temperature independent term $\chi = C/(T - \Theta)$. In the range 200 – 300 K, the fitting the experimental data gives C = 4.6 emu/mol K and $\Theta = -47 \pm 1$ K. The negative value of the Weiss temperature Θ is an indication of prevailing antiferromagnetic exchange interactions. The value of the Curie constant C can be put into correspondence with the effective magnetic moment μ_{eff} as $8C = \mu_{eff}^2$ [20].

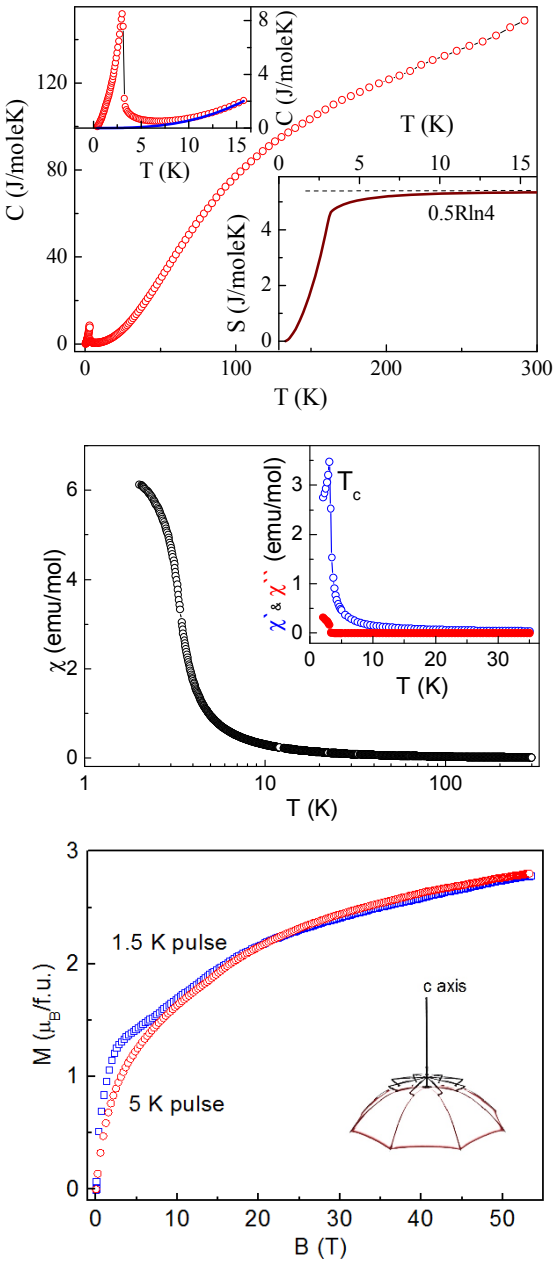

Fig. 4. Upper panel: Temperature dependence of specific heat in $Co(NO_3)_2$. The upper inset enlarges the low temperature region in the vicinity of the phase transition. The lower inset

represents the temperature dependence of magnetic entropy. Middle panel: Temperature dependence of *dc* magnetic susceptibility $\chi = M/B$ in $Co(NO_3)_2$. The inset represents the temperature dependences of both real χ' (upper curve) and imaginary χ'' (lower curve) of *ac* magnetic susceptibility. Lower panel: Pulsed magnetic field dependences of magnetization in $Co(NO_3)_2$ taken in both magnetically ordered ($T < T_N$) and paramagnetic ($T > T_N$) phases. The inset represents the image of inverted umbrella.

The value of $\mu_{eff} = 6.07\ \mu_B$ is much higher than expected for the spin-only contribution $\mu_{spin\text{-}only} = 3.87\ \mu_B$. It signifies a large component of the orbital magnetic moment unquenched in the Co^{2+} ions. On the other hand, the effective moment in the paramagnetic state can be expressed as $\mu_{eff}^2 = ng^2S(S+1)$, where $n = 1$ is the number of the Co^{2+} ions per formula unit. The average *g*-factor value $g = 4.11(2)$ was obtained in the ESR measurements and $S = 3/2$ is the value of spin. Thus, $\mu_{eff} = 7.96(3)\ \mu_B$ is to be expected. The reduction of the effective magnetic moment in the paramagnetic state, i.e. 6.07 μ_B vs. 7.96 μ_B, can be ascribed to single-ion anisotropy of the Co^{2+} ions.

At low temperatures, the $\chi_{dc}(T)$ dependence in $Co(NO_3)_2$ evidences the formation of ferrimagnetic long-range order. The *ac* magnetic susceptibility χ_{ac} taken at alternating field amplitude 3 G and frequency 2000 Hz is shown in the inset to the middle panel of Fig. 4. Sharp singularities in both real χ' and imaginary χ'' components mark the Curie temperature $T_C = 3$ K.

The field dependences of magnetization *M* taken in pulsed magnetic field are shown in the lower panel of Fig. 4. The curve taken at $T < T_N$ evidences a pronounced bending at about 3 T reflecting the domain processes. The magnetization reaches 2.8 μ_B/f.u. at 53.5 T. The magnetization measured at $T > T_N$ smoothly rises with field increase reaching the same value at highest magnetic field. This value is small compared to the saturation value $M_{sat} = ngS\mu_B$, which is about 6.17 μ_B.

First-principles calculations.

To determine the magnetic ground state of $Co(NO_3)_2$, we performed first-principles calculations within local density approximation [21] including spin-orbit coupling for a nonmagnetic and non-collinear spin-polarized states (LDA and LSDA+SO, respectively) as implemented in the Vienna ab-initio simulation package (VASP) [22]. The energy cut-off for the Bloch wavefunctions was set to 500 eV, and the Brillouin zone was sampled by a $10 \times 10 \times 10$ Monkhorst-Pack *k*-point mesh [23]. The effect of electronic correlations of the Co *d*-electrons was taken into account by using the LSDA+*U* method [24], with the on-site Coulomb *U* and intra-atomic exchange *J* interactions 4.0 eV and 1.0 eV, respectively.

As shown in Fig. 5a, the electronic band structure for a nonmagnetic state of $Co(NO_3)_2$ obtained from LDA calculations indicate a set of well isolated bands located near the Fermi level and corresponding to the Co 3*d* state with a contribution from the O 2*p* electrons due to their strong hybridization. These bands form two groups split by the octahedral crystal field by ~0.82 eV.

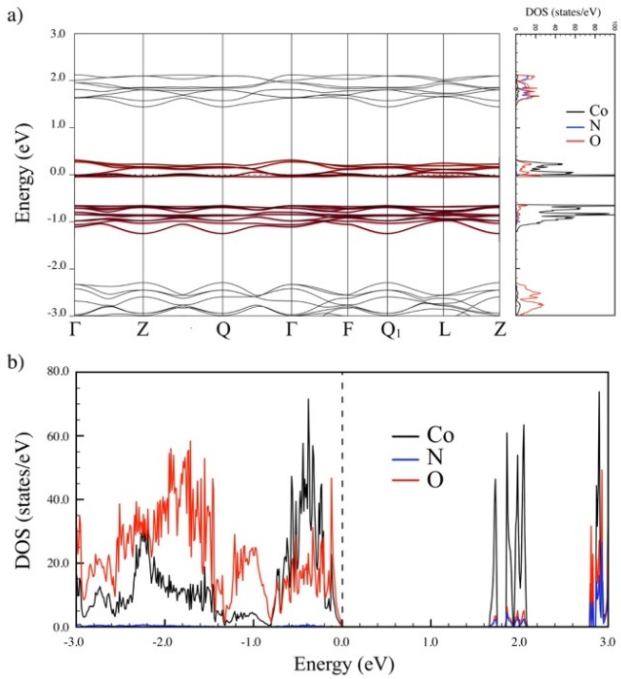

Fig. 5. a) Band structure of $Co(NO_3)_2$ as obtained from LDA calculations. The highlighted bands form a basis for the low-energy electronic model. b) Density of states corresponding to a non-collinear ferrimagnetic configuration of $Co(NO_3)_2$ obtained from LSDA+*U*+SO calculations. The Fermi level is at zero energy.

An insulating behaviour of $Co(NO_3)_2$ is well reproduced in spin-polarized calculations by including electronic correlations of the Co 3*d* states, and the calculated density of states given in Fig. 5b shows an energy gap of 1.63 eV. The corresponding magnetic ground state was found to be a non-collinear inverted umbrella-type configuration, where the magnetic moments at Co2 are ordered ferromagnetically along the *c* axis, while the Co1 magnetic moments are coupled antiferromagnetically to the Co2 sublattice and form a non-coplanar 120°-structure in the *ab* plane with a non-zero scalar spin chirality, $\chi_S = \boldsymbol{S}_1 \cdot (\boldsymbol{S}_2 \times \boldsymbol{S}_3) \neq 0$. Thus, in agreement with the experimental data, the electronic structure calculations reveal an antiferromagnetic coupling between the spins, which is evident in the relative alignment of magnetic moments in the Co1 and Co2 sublattices and responsible for the formation of a non-coplanar magnetic structure. The spin-orbit interaction unquenches the orbital magnetic moments, which are expected to be large for the Co^{2+} ions in the octahedral environment. According to the third Hund's rule, orbital moments tend to align in the same direction as their spin counterparts [24]. The obtained (absolute) values of the spin M^S and orbital M^L magnetic moments are $M^S_{\mathrm{Co1}} \approx M^S_{\mathrm{Co2}} = 2.68\ \mu_B$, $M^L_{\mathrm{Co1}} = 1.18\ \mu_B$ and $M^L_{\mathrm{Co2}} = 1.35\ \mu_B$, and the corresponding net magnetic moments per formula unit are $M^S_{\mathrm{TOT}} = 0.32\ \mu_B$ and $M^L_{\mathrm{TOT}} = 0.11\ \mu_B$. There is a small misalignment of the spin and orbital magnetic moments at the Co1 sites (see Fig. 6a), which is expected if they are oriented away from the high symmetry directions in the crystal [24]. Furthermore, there is also a small contribution (~0.03 μ_B) to the spin magnetic moment coming from each oxygen site.

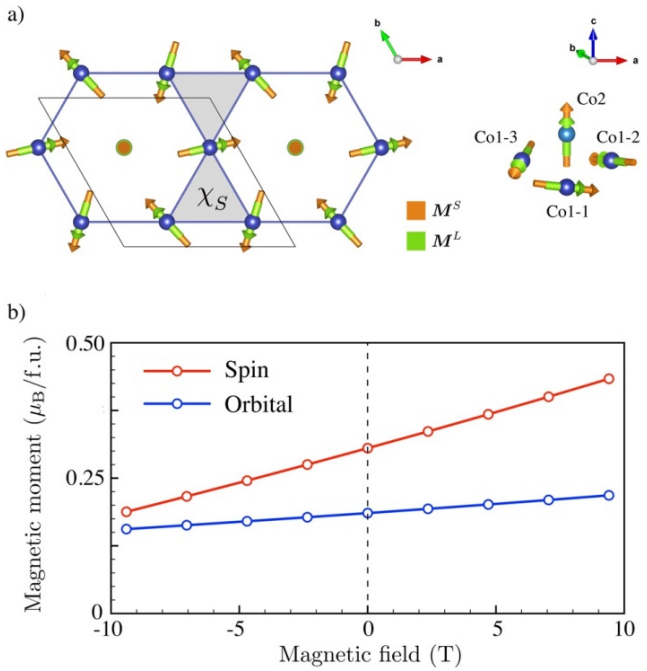

Fig. 6. a) Ferrimagnetic inverted umbrella-type ground state of $Co(NO_3)_2$ and b) dependence of the total spin and orbital magnetic moments (per formula unit) on magnetic field, as obtained from Hartree-Fock calculations. Shaded triangles represent non-zero scalar spin chirality, and the diamond area denotes the unit cell.

To explain the dependence of the magnetic structure on an applied magnetic field, we employed the Hartree-Fock approximation for the low-energy electronic model [25], constructed in the basis of Wannier functions representing the magnetically active bands, as shown in Fig. 5a. To this end, we used the procedure of maximal localization as implemented in the wannier90 package [26]. Matrix elements of the hopping parameters including crystal-field splitting and spin-orbit coupling for the five-orbital model are obtained by projected the LDA Hamiltonian onto the basis of Wannier functions, and parameters of the on-site Coulomb interactions are computed within constrained random phase approximation [27]. Their calculated average values are U = 4.81 (3.67) eV and J = 0.59 (0.61) eV for the Co1 (Co2) atoms. Since the Coulomb repulsion U is different at Co1 and Co2, we had to introduce an additional constraint in the process of calculations enforcing the d^7 electronic configuration at each Co site. The resulting ground-state magnetic structure shown in Fig. 6a is in good agreement with LSDA+U+SO calculations. The corresponding spin and orbital contributions to the magnetic moments are $M^S_{\mathrm{Co1}} \approx M^S_{\mathrm{Co2}} = 2.99\ \mu_B$, $M^L_{\mathrm{Co1}} = 1.17\ \mu_B$ and $M^L_{\mathrm{Co2}} = 1.36\ \mu_B$, and the total spin and orbital moments per formula unit are $M^S_{\mathrm{TOT}} = 0.30\ \mu_B$ and $M^L_{\mathrm{TOT}} = 0.18\ \mu_B$. A small difference from LSDA+U+SO calculations in the spin magnetic moments comes from the fact that the resulting Wannier functions contain both the Co 3d and O 2p contributions due to their hybridization in the magnetically active bands. Finally, when applying a magnetic field along the c axis, one can see that the umbrella-type canting out of the ab plane can be controlled in both directions changing the c axis component of the total spin and orbital magnetic moments that depend almost linearly on the field magnitude. The field dependences of both spin and orbital contributions to the c axis component of Co1 magnetic moments are shown in Fig. 6b.

Conclusion

There is only very narrow range of magnetic field where experimental data and calculations can be compared. $Co(NO_3)_2$ experiences the phase transition into magnetically ordered phase with spontaneous magnetization and forms the domain structure below T_C = 3 K. The pulsed field measurements at 1.5 K reveal firstly increasing magnetization due to the

processes of domain wall displacements and afterwards due to rotation of magnetization within single domains. The rotation of magnetization has been calculated numerically. The slope of experimental $M(B)$ curve in the range 3 – 7 T is $dM/dB \sim 0.05\ \mu_B$/T at $B = 5$ T. This is in a fair agreement with calculated behavior, i.e. sum of the spin contribution, $dM/dB \sim 0.039\ \mu_B$/T, and the orbital contribution, $dM/dB \sim 0.011\ \mu_B$/T. There is no phase boundary between ferrimagnetic and paramagnetic phases in the presence of magnetic field. So, reaching rather modest magnetic field values the magnetization curve exhibits paramagnetic behavior similar to that at 5 K.

In Heisenberg triangular antiferromagnets the frustration of exchange interactions is lifted by formation of 120° chiral structures. The umbrella-type structures are readily observable in Heisenberg triangular antiferromagnets with easy-axis anisotropy in a magnetic field applied along the *c* axis [3]. Ordinarily, this is not a case for Ising antiferromagnets. In $Co(NO_3)_2$, however, the 120° motif appears due to mutual orientation of local easy axes in $Co1O_6$ octahedra. First principles calculations produce comparable values of spin and orbital moments of Co^{2+} ions and establish a non-collinear inverted umbrella-type structure with magnetic moments of umbrella handle Co2 oriented along the *c* axis and magnetic moments of Co1 forming a non-coplanar 120° structure in the *ab* plane with a non-zero scalar spin chirality. This structure turns out to be quite sensitive to external magnetic field allowing for a significant alteration of the *c* axis component of both spin and orbital moments of the Co1 ions. Thus, along with isostructural nickel nitrate, $Co(NO_3)_2$ represents unique case of unconventional chiral non-coplanar ferrimagnet of inverted umbrella type. The single ion anisotropy of Co ions is much larger than that of Ni ions. Accordingly, the magnetization curves in these compounds differ. It follows from the calculations that the umbrella in $Ni(NO_3)_2$ is flat compared to that in $Co(NO_3)_2$.

It is highly desirable to experimentally confirm the calculated magnetic structure and its evolution under magnetic field, which, given the chemical instability of the title compound, seems not easy.

Acknowledgements

This work has been supported by Russian Scientific Foundation, grant 19-42-02010 and by Russian Foundation for Basic Research, grants 18-52-005, 19-02-00015 and 19-03-01059. We acknowledge support by the Russian Ministry of Science and Higher Education, contracts 02.A03.21.0004, 02.A03.21.0006 and 02.A03.21.0011. OVM and ANV acknowledge support by NUST "MISiS", grant K2-2020-008. We acknowledge the support of HLD at HZDR, member of the European Magnetic Field Laboratory (EMFL). BL acknowledges the support of DFG through project B06 of SFB 1143 (ID 247310070). JYL was supported by Taiwan MOST No. 107-2923-M-009-001-MY3 and by the center for Emergent Functional Matter Science of NCTU from the Featured Areas Research Center program within the framework of the Higher education Sprout Project by the Ministry of Education (MOE) in Taiwan. MAH acknowledges the support from the Swedish Research Council (VR) 2018-05339.

References

1. A. P. Ramirez, Ann. Rev. Mater. Sci. **24**, 453 (1994).
2. J. E. Greedan, J. Mater. Chem. **11**, 37 (2001).
3. M. F. Collins and O. A. Petrenko, Can. J. Phys. **75**, 605 (1997).
4. S. Nakatsuji, Y. Nambu, H. Tonomura, O. Sakai, S. Jonas, C. Broholm, H. Tsunetsugu, Y. M. Qiu, and Y. Maeno, Science **309**, 1697 (2005).
5. A. Banerjee, C. A. Bridges, J. Q. Yan, A.A. Aczel, L. Li, M. B. Stone, G. E.Granroth, M. D. Lumsden, Y. Yiu, and J. Knolle, Nat. Mater. **15**, 733 (2016).
6. L. Messio, B. Bernu, and C. Lhuillier, Phys. Rev. Lett. **108**, 207204 (2012).
7. A. A.Tsirlin, A. Moller, B. Lorenz, Y. Skourski, and H. Rosner, Phys. Rev. B **85**, 014401 (2012).
8. O. S. Volkova, V. V. Mazurenko, I. V. Solovyov, E. B. Deeva, I. V. Morozov, J.-Y. Lin C. K. Wen, J. M. Chen, M. Abdel-Hafiez, and A. N. Vasiliev, Phys. Rev. B **90**, 134407 (2014).

9. H. Nakano, T. Shimokawa, and T. Sakai, J. Phys. Soc. Jpn. **80**, 033709 (2011).
10. I. Rousochatzakis, J. Richter, R. Zinke, and A. A. Tsirlin, Phys. Rev. B **91**, 024416 (2015).
11. D. Hoffs, J. Hafner, and D. Spisak, Phys. Rev. B **68**, 014407 (2003).
12. C. C. Addison and N. Logan, Adv. Inorg. Chem. Radiochem. **6**, 71 (1964).
13. G. A. Tikhomirov, K. O. Znamenkov, I. V. Morozov, E. Kemnitz, and S. I. Troyanov Z. Anorg. Allg. Chem. **628**, 269 (2002).
14. K. Momma and F. Izumi , J. Appl. Crystallogr. **44**, 1272 (2011).
15. E. B. Deeva, A. V. Merkulova, S. I. Troyanov, M. A. Zakharov, V. A. Tafeenko, V. F. Kozlovskii and I. V. Morozov, Mendeleev Comm. **26**, 421 (2016).
16. Giester, G., Lengauer, C. L., Wildner, M. & Zemann J., Z. Kristallogr. **223**, 408 (2008).
17. Y. Skourski, M. D. Kuz'min, K. P. Skokov, A. V. Andreev, and J. Wosnitza, Phys. Rev. B **83**, 214420 (2011).
18. A. Abragam and B. Bleaney, EPR of Transition Ions, Clarendon, Oxford, 1970.
19. A. Abragam and M. H. L. Pryce, Proc. R. Soc. A **200**, 173 (1951).
20. P.W. Selwood, Magnetochemistry, 2nd ed., Interscience Pub., New York, 1956.
21. W. Kohn and L. J. Sham, Phys. Rev. A **140**, 1133 (1965).
22. G. Kresse and J. Hafner, Phys. Rev. B **47**, 558 (1993).
23. H. J. Monkhorst and J. D. Pack, Phys. Rev. B **13**, 5188 (1976).
24. I. V. Solovyev, A. I. Liechtenstein, and K. Terakura, Phys. Rev. Lett. **80**, 5758 (1998).
25. I. V. Solovyev, J. Phys.: Condens. Matter **20**, 293201 (2008).
26. A. A. Mostofi, J. R. Yates, G. Pizzi, Y. S. Lee, I. Souza, D. Vanderbilt, and N. Marzari, Comp. Phys. Commun. **185**, 2309 (2014).
27. M. Springer and F. Aryasetiawan, Phys. Rev. B **57**, 4364 (1998).